# Original Articles

# Robust Autofocusing in Microscopy

**Jan-Mark Geusebroek,**[1,2]* **Frans Cornelissen,**[2] **Arnold W.M. Smeulders,**[1] **and Hugo Geerts**[2]

[1]Department of Computer Science, Faculty of Science, University of Amsterdam, Amsterdam, The Netherlands
[2]Life Sciences, Janssen Research Foundation, Beerse, Belgium

**Background:** A critical step in automatic microscopy is focusing. This report describes a robust and fast autofocus approach useful for a wide range of microscopic modalities and preparations.
**Methods:** The focus curve is measured over the complete focal range, reducing the chance that the best focus position is determined by dust or optical artifacts. Convolution with the derivative of a Gaussian smoothing function reduces the effect of noise on the focus curve. The influence of mechanical tolerance is accounted for.
**Results:** The method is shown to be robust in fluorescence, bright-field and phase contrast microscopy, in fixed and living cells, as well as in fixed tissue. The algorithm was able to focus accurately within 2 or 3 s, even under extremely noisy and low contrast imaging conditions.
**Conclusions:** The proposed method is generally applicable in light microscopy, whenever the image information content is sufficient. The reliability of the autofocus method allows for unattended operation on a large scale. Cytometry 39:1–9, 2000. © 2000 Wiley-Liss, Inc.

**Key terms:** autofocusing; focus criteria; focus function; automated microscopy; bright-field microscopy; fluorescence microscopy; phase contrast microscopy

Along with the introduction of high throughput screenings, quantitative microscopy is gaining importance in pharmaceutical research. Fully automatic acquisition of microscope images in an unattended operation coupled to an automatic image analysis system allows for the investigation of morphological changes. Time-lapse experiments reveal the effect of drug compounds on the dynamics of living cells. Histochemical assessment of fixed tissue sections is used to quantify pathological modification.

A critical step in automatic screening is focusing. Fast and reliable autofocus methods for the acquisition of microscope images are indispensable for routine use on a large scale. Autofocus algorithms should be generally applicable on a large variety of microscopic modes and on a large variety of preparation techniques and specimen types.

Although autofocusing is a long standing topic in literature (1–8), no such generally applicable solution is available. Methods are often designed for one kind of imaging mode. They have been tested under well-defined circumstances. The assumptions made for determining the focal plane in fluorescence microscopy are not compatible with the same in phase contrast microscopy, and this holds true throughout. We consider the design of a method that is generally applicable in light microscopy.

From Fourier optics (9) it has been deduced that well-focused images contain more detail than images out of focus. A focus score is used to measure the amount of detail. The focus curve can be estimated from sampling the focus score for different levels of focus. Some examples of focus curves are shown in Figure 2. Best focus is found by searching for the optimum in the focus curve. In a classical approach the value of the focus score is estimated for a few focus positions (4,8,10). Evaluation of the scores indicates where on the focus curve to take the next sample. Repeating the process iteratively should ensure convergence to the focal plane. A major drawback is that such optimization procedure presupposes (a) a unimodal focus function, and (b) a broad-tailed extremum to obtain a wide focus range, which do not hold true in general. In reality, the focus curve depends on the microscope setup, imaging mode and preparation characteristics (11). When the assumed shape of the focus curve does not match the real focus curve, or when local extrema emerge, convergence to the focal plane is not guaranteed.

*Correspondence to: Jan-Mark Geusebroek, Faculty of Science, Department of Computer Science, University of Amsterdam, Kruislaan 403, 1098 SJ Amsterdam, The Netherlands.
E-mail: mark@wins.uva.nl

Groen et al. (2) specifies criteria for the design of autofocus procedures. We adopt these criteria of good focusing: (a) accuracy, (b) reproducibility, (c) general applicability, (d) insensitivity to other parameters. Under insensitivity to other parameters is considered robustness against noise and optical artifacts common to microscopic image acquisition. Further, we reject the criteria of unimodality of the focus curve, which cannot be achieved in practice (11,12). As a consequence, the range or broadness of the extremum in the focus curve is of less relevance.

In this report, an autofocus method is presented which is generally applicable in different microscopic modes. The aim was to develop a method especially suited for an unattended operational environment, such as high throughput screenings. Therefore, the method should be robust against confounding factors common in microscopy, as noise, optical artifacts, and dust on the preparation surface. To evaluate the performance of the autofocus method, experiments have been conducted in screening applications.

## MATERIALS AND METHODS
### The Focus Score

From Fourier optics, measurement of the focus score can best be based on the energy content of a linearly filtered image (2,9). It can be deduced (2,4,11) that an optimal focus score is output by the gradient filter. Scale-space theory (13) leads to the use of the first-order Gaussian derivative to measure the focus score. The $\sigma$ of the Gauss filter determines the scale of prominent features. The focus function becomes

$$F(\sigma) = \frac{1}{NM} \sum_{x,\ y} [f(x,\ y) * G_x(x,\ y,\ \sigma)]^2 +$$

$$[f(x,\ y) * G_y(x,\ y,\ \sigma)]^2 = \frac{1}{NM} \sum_{x,\ y} f_{x^2} + f_{y^2} \qquad (1)$$

where $f(x,y)$ is the image gray value, and $G_x(x,y,\sigma)$, $G_y(x,y,\sigma)$ are the first-order Gaussian derivatives in the $x$- and $y$-direction at scale $\sigma$, $NM$ is the total amount of pixels in the image, and $f_x, f_y$ are the image derivatives at scale $\sigma$ in the $x$- and $y$-direction, respectively.

Often, a trade-off between noise sensitivity and detail sensitivity can be observed for a specific microscope set-up. For example, in fluorescence microscopy the signal-to-noise ratio (SNR) is often low, and relatively smooth images are examined. For phase contrast microscopy, SNR is high, and small details (the phase transitions) have to be detected. Accuracy of autofocusing depends on the SNR as propagated through the focus score filter (8). Therefore, the $\sigma$ of the Gaussian filter should be chosen such that noise is maximally suppressed, while the response to details of interest in the image is preserved. For bar-like structures, the value of $\sigma$ should conform to (14)

$$\sigma \approx d/2\sqrt{3} \qquad (2)$$

where the thickness of the bar is given by $d$. Assuming that the smallest detail to be focused may be considered bar shaped, Eq. (2) gives an indication for the minimal value of $\sigma$. Note that the filter response degrades for smaller values, whereas a very large value smooths all details to noise level.

### Measurement of the Focus Curve

Consider a system consisting of the following hardware: (a) a microscope with scanning stage and position controller for both axial and lateral direction, (b) a camera placed on the microscope recording its field of view, (c) a video digitizer connected to a computer system, writing at video rate the camera output into the computer's memory. The computer system is able to send positioning commands to the stage controller. Examples of such systems will be given later.

The focal plane of the microscope is assumed to be within a pre-defined interval $\Delta z$ around the start $z$-position $z$. The scanning stage is moved down to the position $z_{min} = z - \frac{1}{2}\Delta z$. Backlash correction is applied by sending the stage further down than necessary, and raising it again to the given position (6). In this way, focus positions are always reached from the same direction. As a result, mechanical tolerance in cog wheels is eliminated.

At $t = 0$ ms, the stage controller starts raising the stage to traverse the complete focus interval $\Delta z$. During the stage movement through focus, successive images of the preparation are captured at 40 ms intervals (video rate). The focus score of each captured image is calculated. The image buffer is re-used for the next video frame, necessitating only two image memory buffers to be active at any time. One of the buffers is used for focus score calculation of the previously captured image, while the other is used for capturing the next image. Calculation of the focus score should thus be performed within one video frame time.

As soon as the stage has reached the end of the focus interval, timing is stopped at $t = t_d$ ms. An estimation of the focus curve is obtained for the complete focus interval. The global optimum in the estimate for the focus curve represents the focal plane. Now, each $z$-position is related to the time at which the corresponding image has been captured. When linear movement of the stage is assumed, the position at which the image at time $t$ is taken corresponds to

$$z_i = \frac{t_i}{t_d} \Delta z + z_{min} \qquad (3)$$

where $t_d$ represents the travel duration, $\Delta z$ is the focus interval, and $z_{min}$ is the start position (position at $t = 0$ ms).

Since the focus curve is parabolic around the focal plane (6–8), high focus precision can be achieved by quadratic interpolation. When assuming linear stage

movement, or $z = vt + z_{\min}$, the focus curve around the focal plane can be approximated by

$$s(t) = c + bt + at^2 \qquad (4)$$

The exact focus position is obtained by fitting a parabola through the detected optimum and its neighboring measurements. Consider the detected optimum $s(t_o) = s_o$ at time $t = t_o$. The time axis may be redefined such that the detected optimum is at time $t = 0$. Then, neighboring scores are given by $(s_n, t_n)$ and $(s_p, t_p)$, respectively. Solving for $a$, $b$, and $c$ gives

$$c = s_0, \; b = \frac{-s_0 t_n^2 + s_p t_n^2 + s_0 t_p^2 - s_n t_p^2}{t_n^2 t_p - t_n t_p^2}$$

$$a = \frac{s_0 t_n - s_p t_{n-s_0 t_p + s_n t_p}}{t_n^2 t_p - t_n t_p^2} \qquad (5)$$

The peak of the parabola, and thus the elapsed time to the focus position, is given by

$$t_f = -\frac{b}{2a} + t_0 = \frac{s_0 t_n^2 - s_p t_n^2 - s_0 t_p^2 + s_n t_p^2}{2(s_0 t_n - s_p t_n - s_0 t_p + s_n t_p)} + t_0 \quad (6)$$

The focal plane is at position

$$z_f = (t_f / t_d)\Delta z + z_{\min} \qquad (7)$$

to which is moved, taking the backlash correction into account.

## Sampling the Focus Curve

The depth of field of an optical system is defined as the axial distance from the focal plane over which details still can be observed with satisfactory sharpness. The thickness of the slice which can be considered in focus is then given by (15,16)

$$z_d = \lambda / \left[ 2n \left( 1 - \sqrt{1 - \left(\frac{NA}{n}\right)^2} \right) \right] \qquad (8)$$

where $n$ is the refractive index of the medium, $\lambda$ the wavelength of the used light, and $NA$ the numerical aperture of the objective. The focus curve is sampled at Nyquist rate when measured at $z_d$ intervals (17). The parabolic fitting ensures that focus position is centered within thick specimens, i.e., specimens much larger than $z_d$. Common video hardware captures frames at fixed rate. Thus the sampling density of the focus curve can only be influenced by adjusting the stage velocity to travel $z_d$ μm per video frame time.

In order to calculate the focus score within video frame time for current sensors and computer systems, simplification of the focus function Eq. (1) is considered. For biological preparations, details are distributed isotropically over the image. The response of the filter in one direction is adequate for determination of the focal plane.

Further computation time can be saved by estimating the filter response from a fraction of the scan lines in the image. Then, the focus function is given by

$$F(\sigma) = \frac{L}{NM} \sum_{x,y} [f(x, \; y) * G_x(x, \; y, \; \sigma)]^2. \qquad (9)$$

For our purpose, each sixth row ($L = 6$) is applied. A recursive implementation of the Gaussian derivative filter is used (18), for which the computation time is independent of the value of $\sigma$. The calculation time is kept under 40 ms for all computer systems we used in the experiments, even when the system is running other tasks simultaneously. Comparison between the focus curve calculated in two dimensions for the whole image [Eq. (1)], and the response of Eq. (9) reveals only marginal differences for all experiments.

## Large, Flat Preparations

For the acquisition of multiple aligned images from large, flat preparations, the variation in focus position is assumed small but noticeable at high magnification. Proper acquisition of adjacent images can be obtained by focusing a few fields. Within the preparation, the procedure starts by focusing the first field. Fields surrounding the focused field are captured, until the next field to capture is a given distance away from the initially focused field. Deviation from best focus is now corrected for by focusing over a small interval. The preparation is scanned, keeping track of focus position at fields further away than a given distance from the nearest of all the previously focused fields. The threshold distance for which focusing is skipped depends on the preparation flatness and magnification and has to be empirically optimized for efficiency. Fields that have been skipped for focusing are positioned at the focus level of the nearest focused field. Small variations in focus position while scanning the preparation are corrected during acquisition.

## Preparation and Image Acquisition

The autofocus algorithm is intensively tested in the following applications: (a) quantitative neuronal morphology, (b) time-lapse experiments of cardiac myocyte dedifferentiation, (c) immunohistochemical label detection in fixed tissue, (d) *C. elegans* GFP-VM screening, (e) acquisition of smooth muscle cells, and (f) immunocytochemical label detection in fixed cells. Each of these applications is described below. The software package SCIL-Image version 1.4 (19) (TNO-TPD, Delft, The Netherlands) is used for image processing, extended with the autofocus algorithm and functions for automatic stage control and image capturing. All preparations are observed on Zeiss invert microscopes (Carl Zeiss, Oberkochen, Germany), except for the immunohistochemical label detection, which is observed with a Zeiss Axioskop. The wavelength of the used light is 530 nm, unless stated differently. For automatic position control, the microscopes are equipped with a scanning stage and MAC4000 or (comparable)

Table 1
*Summary of the Experimental Setup and Parameter Settings for the Various Experiments**

| Application | Mode | Obj | (NA) | $\sigma$ | (d) | $\Delta z$ | $z_d$ | $v_{eff}$ | Area | (Images) | Backlash |
|---|---|---|---|---|---|---|---|---|---|---|---|
| Quant neuronal morph | bright | 5× | (0.15) | 1.0 | (3) | 500 | 23.6 | 24.7 | 6.7 × 6.7 | (8 × 8) | — |
| Cardiac myocyte dediff | phase | 32× | (0.4) | 1.0 | (4) | 100 | 3.3 | 2.5 | 6 × 1 field | | 15 |
| Immunohist label det | bright | 2.5× | (0.075) | 1.0 | (3) | 1,000 | 94 | 98.7 | complete slice | | — |
| *C. elegans* screening | fluoresc | 40× | (0.6) | 8.5 | (30) | 50 | 1.47 | 4.94 | complete well | | 15 |
| Acq smooth muscle | phase | 10× | (0.3) | 1.0 | (4) | 500 | 5.89 | 4.94 | 5 × 5 | (12 × 12) | 10 |
| Immunocyt label det | fluoresc | 40× | (0.6) | 8.5 | (30) | 250 | 1.25/1.67 | 4.94 | 1.2 × 1.2 | (5 × 5) | 15 |

*The value for $\sigma$ [Eq. (2)] is given together with the smallest structure (d) in pixels. The focus interval $\Delta z$ and depth of field $z_d$ are given in $\mu$m. The effective velocity used during focusing is given by $v_{eff}$ in $\mu$m/40 ms. The covered area within the preparation is given in mm$^2$. Backlash correction is given in $\mu$m.

MC2000 controller (Märzhäuser, Wetzlar, Germany). At power on, the stage is calibrated and an initial focus level is indicated manually. Backlash correction is empirically determined. For each application, the focus interval $\Delta z$ is determined by evaluating the variability in the $z$-position between focus events.

## Quantitative Neuronal Morphology in Bright-Field Mode

Morphological changes of neurons are automatically quantified as described in Nuydens et al. (20). Briefly, PC12 cells were plated in poly-L-lysine (Sigma, St. Louis, MO) coated 12-well plates. In each well $5 \times 10^4$ cells were seeded. After 24 h the cells were fixed with 1% glutaraldehyde for 10 min. Then the cells were washed twice with distilled water. The plates were dried in an incubator.

The plates are examined in bright-field illumination mode, for details see Table 1. The camera used is an MX5 (Adaptec, Eindhoven, The Netherlands) 780 × 576 video frame transfer CCD with pixel size 8.2 × 16.07 $\mu$m$^2$, operating at room temperature with auto gain turned off. Adjacent images are captured by an Indy R4600 132 MHz workstation (Silicon Graphics, Mountain View, CA), resulting in an 8 × 8 mosaic image for each well. Prior to the acquisition of the well, autofocusing at the center of the scan area is performed. The smallest details to focus are the neurites, which are about 3 pixels thick, yielding $\sigma = 1.0$ [Eq. (2)]. The wavelength of the illumination is about 530 nm, resulting in 23.4 $\mu$m depth of field [Eq. (8)]. The effective stage velocity is somewhat different due to rounding off to controller built-in speeds. Due to the low magnification, backlash correction is not necessary.

## Cardiac Myocyte Dedifferentiation in Phase Contrast Mode

Cardiac myocytes were isolated from adult rats ($\approx$250 g) heart by collagenase perfusion as described in (21). The cell suspension containing cardiomyocytes and fibroblasts was seeded on Laminin-coated plastic petri dishes, supplied with M199 and incubated for 1 h. Thereafter, unattached and/or dead cells were washed away by rinsing once with M199. The petri dishes were filled with M199 + 20% fetal bovine serum and incubated at 37°C.

The petri dishes are examined in phase contrast mode, for details see Table 1. During the experiment, ambient temperature is maintained at 37°C. Time-lapse recordings (15 h) are made in six manually selected fields, one in each of the six petri dishes. The scanning stage visits the selected fields at 120-s intervals. Fields are captured using a CCD camera (TM-765E, Pulnix, Alzenau, Germany). They are added to JPEG compressed digital movies (Indy workstation with Cosmo compressor card, SGI, Mountain View, CA), one for each selected field. Autofocusing is applied once per cycle, successively refocusing all the fields in six cycles. The smallest details to focus are the cell borders.

## Immunohistochemical Label Detection in Bright-Field Mode

Sections of the amygdala of mice injected with a toxic compound were cut at 15 $\mu$m thickness through the injection site. They were subsequently immunostained for the presence of the antigen, using a polyclonal antibody (44-136, Quality Control Biochemicals Inc., Hopkinton, MA) and visualized using the chromogen DAB.

Four microscope slides (40 brain slices) at once are mounted on the scanning stage and observed in bright-field illumination mode (see Table 1). Adjacent images are captured (Meteor/RGB frame-grabber, Matrox, Donval, Quebec, Canada in an Optiplex GXi PC with Pentium 200MHz MMX, Dell, Round Rock, TX) by use of an MX5 CCD camera (Adaptec, Eindhoven, The Netherlands). As a result, mosaics of complete brain slices are stored on disk. Prior to acquisition, autofocusing at approximately the center of the brain slice is performed, the smallest details to focus being tissue structures. Due to the low magnification, backlash correction is not necessary.

## *C. elegans* GFP-VM Screening in Fluorescence Mode

Individual *C. elegans* worms transgenic for GFP expressing vulval muscles (GFP-VM) were selected from stock, and one young adult hermaphrodite ($P_0$) was placed in each of the 60 center wells of a 96-well plate (Costar, Acton, MA) filled with natural growth medium, and incubated for 5 days at 25°C to allow $F_1$ progeny to reach adult stage.

Before image acquisition, fluorescent beads (F-8839, Molecular Probes, Eugene, OR) are added to the wells as background markers for the focus algorithm. The well plate is examined in fluorescence mode, see Table 1. A

FITC filter (B, Carl Zeiss, Oberkochen, Germany) in combination with a 100-W Xenophot lamp is used to excite the GFP. Images are captured (O2 R5000 180 MHZ workstation, Silicon Graphics, Mountain View, CA) using an intensified CCD camera (IC-200, PTI, Monmouth Junction, NJ). Each of the selected wells is scanned and the adjacent images, completely covering the well, are stored on disk. Variability in the $z$-position between the center of the wells turned out to be within 250 μm, which is taken as focus interval for initial focusing. After autofocusing on the well center, deviation from best focus while scanning the well is corrected over one-fifth of the initial focus interval. Focusing of all fields further than three fields away from a focused field was sufficient to keep track of the focal plane. The diameter of the fluorescent spheres is 15 μm (30 pixels), which is much larger than $z_d$. Since the spheres are homogeneously stained, the smallest detail to consider in the $z$-direction is a cylindrically shaped slice through the spheres, where the cylinder height is determined by the horizontal resolution. Therefore, stage velocity is reduced to approximately one-third of the sphere diameter during focusing.

## Acquisition of Smooth Muscle Cells in Phase-Contrast Mode

Smooth muscle cells were enzymatically isolated from the circular muscle layer of guinea pig ileum by a procedure adapted from Bitar and Makhlouf (22). Dispersed cells were suspended in a HEPES buffered saline containing 1 mM $CaCl_2$. Aliquots (200 μl) of the cell suspension were distributed over test tubes and maintained at 37°C for 30 min. Then, 800 μl of medium containing the compound to be tested was added, and cells were incubated for 30 s. The reaction was stopped by addition of 1% glutaraldehyde.

A drop of each cell suspension is brought on a microscopic glass slide, and observed in phase contrast mode (see Table 1). A region containing sufficient cells is selected manually, and adjacent images are captured (Indy R4600 132MHz workstation, Silicon Graphics, Mountain View, CA) using an MX5 CCD camera (Adaptec, Eindhoven, The Netherlands). Autofocusing is performed at approximately the center of the selected area, the smallest details being the elongated cells.

## Immunocytochemical Label Detection in Fluorescence Mode

Human fibroblasts were seeded in a 96-well plate (Costar, Acton, MA) at 7000 cells per well, in 2% FBS/Optimem. Cells were immunostained according to Henkel et al. (23) with primary antibody rabbit anti-human NF-$_\kappa$B (p65) (Santa Cruz Biotechnology, Santa Cruz, CA) and secondary Cy3 labeled sheep anti-rabbit (Jackson, Uvert-Grove, PA). Further, nuclear counter staining with Hoechst 33342 (Molecular Probes, Eugene, OR) was applied.

Well plates are examined in fluorescence mode, see Table 1. A DAPI/FITC/TRITC filter (XF66, Omega Optical, Brattleboro, VT) in combination with a 100 W Xenophot
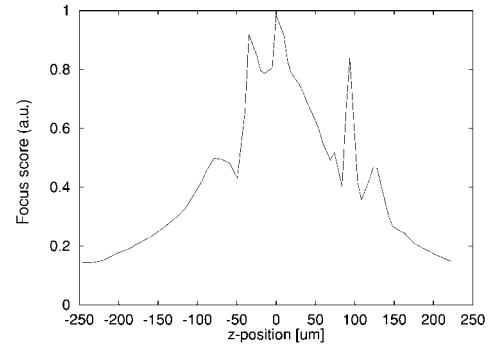


FIG. 1. Focus function as measured for the smooth muscle cells in phase contrast mode. The focus score (arbitrary units) of one representative field is plotted as a function of the $z$-position. The peaks are caused by phase transition effects; the focal plane for the cell bodies is at −75 μm.

lamp is used to excite the cells (emission nuclei at 450 nm, immuno signal at 600 nm). Adjacent images are captured (O2 workstation R5000 180MHZ, Silicon Graphics, Mountain View, CA) using an intensified CCD camera (IC-200, PTI, Monmouth Junction, NJ). Autofocusing is performed at approximately the center of the scan area, the smallest details being the nuclei. Cell thickness is about 5–15 μm, much larger than $z_d$. Therefore, during focusing, stage velocity is reduced to approximate the cell thickness.

## Evaluation of Performance for High NA

The autofocus algorithm performance is objectively evaluated by comparing focus random error with observers. For this purpose, 2 μm Epon sections of dog left ventricle cardiac myocytes stained with periodic acid–Schiff and toluidine blue are observed with a Zeiss Axioplan. A high NA objective 40× NA 1.4 oil immersion is used, for which the depth of field is $z_d = 0.36$ μm [Eq. (8)]. Autofocusing is considered not trivial under these circumstances. Unfocused, arbitrarily selected fields (20 in total) are visited and manually focused by two independent experienced observers. Focus positions are recorded for both observers. Similarly, the found focus positions for the autofocus algorithm is recorded (σ = 1.0, backlash correction 15 μm, $\Delta z = 25$ μm). Comparison of the random error between observers and for observer versus autofocus gives an objective evaluation of autofocus performance.

## RESULTS
## Autofocus Performance Evaluation

The focus algorithm was not able to focus accurately on the smooth muscle cells. Figure 1 shows a representative focus curve measured with σ = 1.0. Measurement of the focus curve at other scales resulted in similar curves. The peaks are caused by phase transitions occurring when scanning through focus. For different focus positions, bright halos appear around the cells due to light diffraction (12). The area of the cell bodies is small compared to
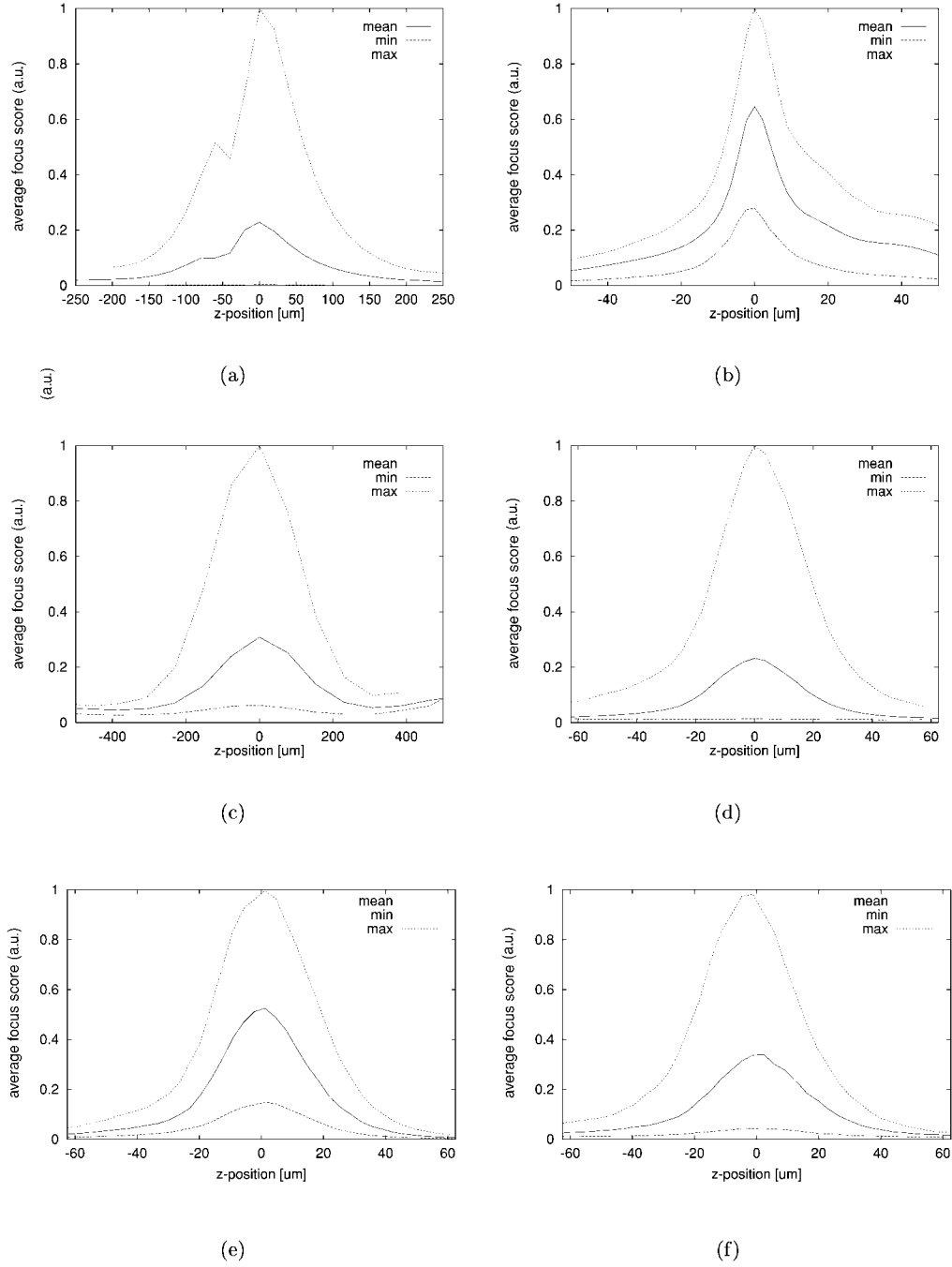
FIG. 2. Average focus score (arbitrary units) as function of the $z$-position measured for different applications. **(a)** Quantitative neuronal morphology, **(b)** cardiac myocyte dedifferentiation, **(c)** immunohistochemical label detection, **(d)** *C. elegans* GFP-VM screening, **(e)** and **(f)** immunocytochemical label detection nuclei and immuno signal, respectively. The measured focus curves indicated by "max" and "min" represent the focus events resulting in the highest and lowest maximum score, indicating variability and influence of noise on the estimate of the focus score.

the size of the halos, and thus the relevant image information content is too low. These circumstances caused failure of the focus algorithm to accurately focus on the cell bodies.

For the other applications, Figure 2 shows the average focus curves, not considering complete failures. The variation in focus score is mainly due to the different number of cells or amount of tissue present in each field. For the time lapse of the cardiac myocytes (Fig. 2b), variation in focus score is caused by the dedifferentiation of the cardiac myocytes over time. The variation in focus score for the immunohistochemical label detection (Fig. 2c) is caused by contrast differences between slices. Further, for the quantitative neuronal morphology (Fig. 2a), the mea-

Table 2
*Summary of the Results for the Various Experiments\**

| Application | Mode | No. of events | Failures | (% Correct) | $t_{foc}$ | % $t_{acq}$ | ($t_{acq}$) |
|---|---|---|---|---|---|---|---|
| Quant neuronal morph | bright | 180 | 0 | (100) | 1.7 | 7.5 | (4.5 min) |
| Cardiac myocyte dediff | phase | 75 | 0 | (100) | 2.8 | | — |
| Immunohist label det | bright | 100 | 2 | (98) | 1.5 | 7 | (3 min) |
| *C. Elegans* screening | fluoresc | 1800 | 14 | (>99) | 1.1 | 12 | (4.5 h) |
| Immunocyt label det | fluoresc | 300 | 2 | (>99) | 2.8 | 14 | (20 min) |

*The total number of focus events is denoted by no. of events. The time needed for focusing is given by $t_{foc}$ in seconds, and as percentage of the total acquisition time $t_{acq}$.

sured focus curve with lowest maximum score (peak at 0.004) is at a field containing only some dead cells. Note the local maximum beneath focus, caused by a 180° phase shift in the point spread function of the optical system (24).

Table 2 shows a summary of autofocus performance. All fields were accurately focused according to an experienced observer, except for a few complete failures. Focus could not be determined on empty fields, as is the case for 14 failures in the *C. elegans* GFP-VM screening. For the immunohistochemical label detection, focusing failed on two fields, which contained not enough contrast for focusing. Further, for two fields in the immuno signal of the immunocytochemical label detection, the camera was completely saturated (bloomed) due to preparation artifacts, causing the autofocus algorithm to fail. For the *C. elegans* GFP-VM screening, total acquisition time for a 96-well plate was 4.5 h for 28,000 images, which is reasonable given the time needed for preparation.

In summary, failure is caused by a shortage of relevant image information content. The proposed algorithm was completely successful in determining correct focus position for the thoroughly stained preparations of the quantitative neuronal morphology, even for fields containing only a few dead cells. Further, complete success was achieved for the cardiac myocyte dedifferentiation. Despite the morphological changes in image content during the experiment, none of the time lapse movies was out of focus any time. A high success rate was obtained for the immunohistochemical label detection, failing for two fields containing not enough contrast. For the fluorescence applications, the images were highly degraded by the presence of random noise (SNR ≤ 10 dB) due to fluorescent bacteria (*C. elegans* screening), camera noise, and structural noise caused by earth loops in combination with the extremely sensitive CCD camera. Nevertheless, a high success rate was achieved.

### Evaluation of Performance for High NA

Comparison between observer 1 and observer 2 resulted in an average error of 0.070 μm, whereas autofocus versus observer 1 resulted in 0.423 μm error. Hence, the autofocus method as implemented is slightly biased. The root mean squared error was 0.477 μm between observers, and 0.494 μm between autofocus and observer, which are both in the range of the depth of field for the used objective. Maximum error between observers was

1.27 μm, and for autofocus versus observer 1.12 μm, both within the slice thickness of 2 μm. Concluding, even for high NA objectives, autofocus performance is comparable to experienced observers.

### Comparison of Performance With Small Derivative Filters

In order to evaluate the effect of the scale σ in the estimate for the focus score, experiments with σ = 0.5 are performed.

For the quantitative neuronal morphology, accurate focusing with σ = 0.5 was not possible for 1 out of 24 fields. In this case, the algorithm focused on the reversed phase contrast image. Application of the small scale in focusing of the cardiac myocyte dedifferentiation failed whenever fungal contamination at the medium surface occurred, which was taken as focal plane. Taking σ = 1.0 solved this problem, that is by focusing persistently on the myocytes. Focusing with σ = 0.5 on the immunohistochemical label detection resulted in focusing on dust particles at the glass surface for 5 out of 24 fields. For the fluorescence applications, accurate focusing was not possible with σ = 0.5, due to the small signal to noise ratio (SNR ≤ 10 dB). Experiments taken with σ = 0.75 resulted in inaccurate focusing for 18 out of 30 fields for the *C. elegans* GFP-VM screening. Further, the algorithm was not able to focus accurately on 13 out of 30 fields for the nuclei in the immunocytochemical label detection, and failed for 17 out of 30 fields on the immuno signal. Repeating these experiments with the values of σ as given in Table 1 resulted in accurate focus for all fields.

### General Observations

The effect of the scale σ results in robustness against noise and artifacts. A larger scale resulted in robustness against phase reversion (quantitative neuronal morphology), fungal contamination at the medium surface (cardiac myocyte dedifferentiation), dust on the glass surface (immunohistochemical label detection), and noise (the fluorescence applications). The performance of small differential filters (2,8,10,11) is poor given the number of inaccurately focused images for σ = 0.5 or σ = 0.75.

For the different applications, the chosen focus interval was effectively used for about 30%, i.e., the top of the measured focus curve was commonly within one-third of the focus interval centered at the origin. The focus interval should not be taken too narrow to ensure that the focal

plane is inside the interval, regardless manual placement of the preparations. An effective use of 30% of the interval for 95% of the focus events seems an acceptable rule of thumb.

The time needed for the autofocus algorithm varied from 1.5 s up to 2.8 s for current sensors and computer systems, which is in the same time range as experienced observers. Focus time is completely determined by the depth of field and the video frame time, which both can be considered as given quantities, and by the size of the focus interval. Therefore, further reduction of focus time can only be achieved by a smaller focus interval, on the condition that the variability in preparation position is limited. When positional variability is low or well known, the focus interval $\Delta z$ can be reduced to exactly fit the variability. For the applications given, focus time can be reduced up to a factor 3 in this way.

Failure of the autofocus algorithm due to a shortage of image content can be well predicted. If the focal plane is inside the focus interval, there should be a global maximum in the estimate of the focus curve. Comparing the maximum focus score $s_o$ with the highest of the focus scores at the ends of the focus interval, $s_e = \max(s(0), s(t_d))$, which are certainly not in focus, determines the signal content with respect to noise. When the maximum score does not exceed significantly the focus scores at the ends of the interval, or $(s_o - s_e)/s_e < \alpha$, the found focus position should be rejected. In this case, focusing can better be based on a neighboring field. For the reported results, a threshold of $\alpha = 10\%$ safely predicts all failures.

## DISCUSSION

The success of automatic morphological screenings holds or falls with the accuracy of autofocus procedures. Although focusing is trivial for a trained observer, automatic systems often fail to focus images in different microscopic modalities. Autofocus procedures are often optimized for one specific preparation, visualized in one microscopic imaging mode. This report presents a method for autofocusing in multi-mode light microscopy. The objective was to develop a focus algorithm which is generally applicable in microscopy, and robust against confounding factors common in microscopy.

Defocused images inherently have less information content than well focused images (2,4). Focus functions based on this criteria, such as the Gaussian derivative filter used in the presented method, by definition respond to the best focus position with a local maximum. Reliable focusing, without taking a priori information into account, is possible whenever the best focus response becomes the global maximum. This criterion is fulfilled when the information content due to the signal is higher than that of optical artifacts, inherent to some modes of microscopic image formation, and noise. Sampling of the focus curve at Nyquist rate over the complete focal range guarantees detection of the global maximum. Consequently, the present autofocus method is generally applicable in any microscopic mode, whenever the amount of detail in the preparation is of larger influence than artifacts and noise.

The effectiveness of the proposed method has been evaluated experimentally for the following specimen: neuronal cells in bright field, cardiac myocytes in phase contrast, neuronal tissue sections in bright-field, fluorescent beads and GFP-VM expressing C. Elegans Nematodes, smooth muscle cells in phase contrast, and immunocytochemically fluorescent-labeled fibroblasts. The method was not able to focus the smooth muscle cells accurately, due to a lack of relevant image information content. For the other experiments, 2830 fields were focused with an overall success rate of 99.4%, where of the remaining 0.6% failure could be safely predicted. For each new specimen and microscope set-up, it suffices to set the parameters for scale $\sigma$, focus interval $\Delta z$, and focus speed, which can be derived from the size of the structures in the specimen, the used light and objective NA. In addition, for the scanning of large preparation, the distance after which focus has to be corrected and the fraction of the focus interval to correct for should be set.

In contrast to other autofocus methods, the proposed algorithm is robust against confounding factors like: (a) noise, (b) optical artifacts, inherent to a particular mode of microscopic image formation, as halos in phase-contrast microscopy, and (c) artifacts such as dust and fungal contamination, lying at a different focus level than the preparation. Focusing is performed within 2 or 3 s, which is in the same time range as trained observers. Moreover, even for high NA objectives, autofocus accuracy is comparable to experienced observers. For high magnification imaging of thick specimens, the method can be easily combined with focal plane reconstruction techniques (25,26).

No constraints have been imposed on the focus curve other than that the global maximum indicates the focal plane. Hence, the method is generally applicable in light microscopy. The reliability of the proposed autofocus method allows for unattended operation on a large scale.

## LITERATURE CITED

1. Firestone L, Cook K, Culp K, Talsania N, Preston K. Comparison of autofocus methods for automated microscopy. Cytometry 1991; 12: 195–206.
2. Groen FCA, Young IT, Ligthart G. A comparison of different focus functions for use in autofocus algorithms. Cytometry 1985; 6:81-91.
3. Johnson ET, Goforth LJ. Metaphase spread detection and focus using closed circuit television. J Histochem Cytochem 1974;22:536–545.
4. Krotkov E. Focusing. Int J Computer Vision 1987;1:223–237.
5. Lockett SJ, Jacobson K, Herman B. Application of 3D digital deconvolution to optically sectioned images for improving the automatic analysis of fluorescent-labeled tumor specimens. Proc SPIE 1992; 1660:130–139.
6. Mason DC, Green DK. Automatic focusing of a computer-controlled microscope. IEEE Trans Biomed Eng 1975;22:312–317.
7. Mendelsohn ML, Mayall BH. Computer-oriented analysis of human chromosomes-iii: Focus. Comput Biol Med 1971;2:137–150.
8. Subbarao M, Tyan JK. Selecting the optimal focus measure for auto-

focusing and depth-from-focus. IEEE Trans Pattern Anal Machine Intell 1998;20:864–870.

9. Papoulis A. The Fourier Integral and Its Applications. New York: McGraw-Hill; 1960. 318 p.

10. Boddeke FR, van Vliet LJ, Netten H, Young IT. Autofocusing in microscopy based on the OTF and sampling. Bioimaging 1994;2:193–203.

11. Price JH, Gough DA. Comparison of phase-contrast and fluorescence digital autofocus for scanning microscopy. Cytometry 1994;16:283–297.

12. Pluta M. Advanced Light Microscopy, vol 2. Amsterdam: Elsevier; 1989. 494 p.

13. ter Haar Romeny BM. Geometry-driven diffusion in computer vision. Boston: Kluwer Academic Publishers; 1994. 439 p.

14. Steger C. An unbiased detector of curvilinear structures. IEEE Trans Pattern Anal Machine Intell 1998;20:113–125.

15. Pluta M. Advanced light microscopy, vol 1. Amsterdam: Elsevier; 1988. 464 p.

16. Young IT, Zagers R, van Vliet LJ, Mullikin J, Boddeke F, Netten H. Depth of focus in microscopy. In: Proceedings SCIA'93. Tronto, Norway; 1993. p 493–498.

17. Streibl N. Depth transfer by an imaging system. Opt Acta 1984;31:1233–1241.

18. van Vliet LJ, Young IT, Verbeek PW. Recursive Gaussian derivative filters. In: Proceedings ICPR '98. IEEE Computer Society Press; 1998. p 509–514.

19. van Balen R, Koelma D, ten Kate TK, Mosterd B, Smeulders AWM. ScilImage: A multi-layered environment for use and development of image processing software. In: Christensen HI, Crowley JL, editors, Experimental environments for computer vision image processing. Singapore: World Scientific Publishing; 1994. p 107–126.

20. Nuydens R, Heers C, Chadarevian A, de Jong M, Nuyens R, Cornelissen F, Geerts H. Sodium butyrate induces aberrant tau phosphorylation and programmed cell death in human neuroblastoma cells. Brain Res 1995;688:86–94.

21. Donck LV, Pauwels PJ, Vandeplassche G, Borgers M. Isolated rat cardiac myocytes as an experimental model to study calcium overload: The effect of calcium-entry blockers. Life Sci 1986;38:765–772.

22. Bitar KN, Makhlouf GM. Receptors on smooth muscle cells: characterization by contraction and specific antagonists. J Physiol 1982;242:G400–407.

23. Henkel T, Zabel U, van Zee K, Muller JM, Fanning E, Baeuerle PA. Intramolecular masking of the nuclear location signal and dimerization domain in the precursor for the p50 NF-$_\kappa$B subunit. Cell 1992;68:1121–1133.

24. Young IT, Gerbrands JJ, van Vliet LJ. Fundamental image processing. Delft: Delft University of Technology; 1995. 110 p.

25. Whu HS, Barbara J, Gil J. A focusing algorithm for high magnification cell imaging. J Microsc 1996;184:133–142.

26. Yeo TTE, Ong SH, Jayasooriah, Sinniah R. Autofocusing for tissue microscopy. Imaging Vision Comput 1993;11:629–639.